Comparison of mode II delamination behaviours in multidirectional and unidirectional composite laminates

Tu, Wenjie; Pascoe, John Alan; Alderliesten, René

DOI
10.1016/j.compositesb.2024.111941

Publication date
2025

Document Version
Final published version

Published in
Composites Part B: Engineering

Composites Part B 291 (2025) 111941

Contents lists available at ScienceDirect

Composites Part B

journal homepage: www.elsevier.com/locate/composites

Comparison of mode II delamination behaviours in multidirectional and unidirectional composite laminates

Wenjie Tu *, John-Alan Pascoe, René Alderliesten

Department of Aerospace Structures and Materials, Faculty of Aerospace Engineering, Delft University of Technology, Kluyverweg 1, Delft, 2629HS, The Netherlands

ARTICLE INFO

Dataset link: https://doi.org/10.4121/72b67fbb-dd92-41b0-8d16-bf7679df01b0.v1

Keywords:
Delamination
Polymer–matrix composites (PMC)
Fracture toughness
Fibre bridging
Fractography

ABSTRACT

Multidirectional (MD) composite laminates are extensively employed in structural applications owing to their superior mechanical characteristics. Nevertheless, the evaluation of the fracture toughness of composite laminates primarily relies on tests using unidirectional (UD) specimens. This study evaluates the reliability of characterizing mode II delamination behaviour in MD laminates by using UD specimens. The quantification of delamination area through Digital Image Correlation (DIC) analysis is integrated with a physical Energy Release Rate (ERR) method to ascertain the fracture resistance, which is compared with the ERR derived via a modified J-integral method and the standardized compliance methods. Fractographic analysis reveals similar fracture mechanisms in specimens with identical interfaces. The physical ERR increases notably due to large-scale fibre bridging induced by fibre nesting at 0°//0° interfaces. Conversely, in 0°//90° interfaces, large-area matrix cracking enhances the intrinsic fracture resistance, excluding the extrinsic toughening provided by fibre bridging.

1. Introduction

The formation and development of delamination in composite structures is one of the most damage that significantly compromises structural integrity [1,2]. In order to enhance the damage tolerance design and certification process for composite materials, testing standards have been established to provide guidelines for determining fracture resistance under various fracture modes [3–5]. The recommended data reduction methods are established based on Linear Elastic Fracture Mechanics (LEFM) and the use of unidirectional (UD) laminates. However, multidirectional (MD) composite laminates are more commonly used in engineering structures [6]. When the laminate layup or the interfaceproperties have a substantial effect on the delamination behaviour [7–12], the validity of utilizing UD tests to determine fracture resistance has to be confirmed.

Experimental and numerical studies have been conducted to explore the disparities in delamination behaviours between MD and UD laminates under varying loading conditions [13–20]. For mode I delamination growth in MD laminates, a tortuous delamination path, induced by through-thickness matrix cracking at interfaces with various fibre orientations ($0//\theta$, or $\theta//\theta$), causes different degrees of fibre bridging effects, thereby enhancing fracture resistance compared to UD laminates [21–23]. In mode II, the rising fracture resistance (R-curve) is primarily ascribed to the toughening mechanism prompted by delamination migration at one or multiple interfaces [15,24].

The through-thickness matrix cracking occurs as a result of compelling the delamination to propagate along the longitudinal direction of the specimen, at an angle to the ply orientation. The crack growth terminates at an interface where the directing ply orientation aligns with the longitudinal growth direction under mode II loading [15,25]. This phenomenon closely resembles the damage scenarios observed in composite panels subjected to out-of-plane impact, wherein delamination growth tracks the fibre orientation and migration is impeded [26–28]. In this instance, understanding the delamination behaviour at a $0//\theta$ interface without migration effects can provide a more accurate characterization for delamination behaviour in real structures. Nevertheless, the majority of studies focus on the influence of different interface angles on enhancing fracture resistance by permitting migration.

In addition to the effects of interface properties, the overall stiffness of the laminate also demonstrated significant influence on mode I delamination behaviour. A stiffer specimen yields a larger fibre bridging zone and thus a higher fracture resistance [29]. For MD and UD laminates with the same number of layers and interface angles, disparity in the overall stiffness between them should be deemed influential to fracture resistance. However, an earlier investigation on the effects of thickness on fracture toughness revealed no significant correlation in both mode I and mode II tests [30]. To the authors' knowledge, the

* Corresponding author.
E-mail address: W.Tu@tudelft.nl (W. Tu).

https://doi.org/10.1016/j.compositesb.2024.111941
Received 19 June 2024; Received in revised form 4 October 2024; Accepted 4 November 2024
Available online 19 November 2024

Table 1
Specimen configurations of ELS tests.

Specimen	Interface	Layup	E_f (MPa)	Δ_{clamp} (mm)	a_0 (mm)	L (mm)	B (mm)	h (mm)
UD(0//0)	0°//0°	$[0_8//0_8]$	114 276	7.60	55.0 ± 1.5	90	19.9 ± 0.1	1.29 ± 0.01
UD(0//90)	0°//90°	$[0_7/90//0_8]$	111 440	3.83	55.0 ± 2.0	90	20.0 ± 0.1	1.27 ± 0.01
UD(90//90)	90°//90°	$[0_7/90//90/0_7]$	108 990	3.48	54.0 ± 1.5	90	20.0 ± 0.1	1.27 ± 0.01
MD(0//0)	0°//0°	$[0/90/45/-45]_s//[0/90/45/-45]_s$	52 507	4.68	55.0 ± 2.0	90	19.8 ± 0.1	1.28 ± 0.01
MD(0//90)	0°//90°	$[90/0/45/-45]_s//[0/90/45/-45]_s$	45 977	5.75	56.0 ± 1.0	90	19.8 ± 0.1	1.29 ± 0.01
MD(90//90)	90°//90°	$[90/0/45/-45]_s//[90/0/45/-45]_s$	44 498	6.38	54.5 ± 1.5	90	19.8 ± 0.1	1.30 ± 0.01

Symmetrical laminates are denoted by $_S$ and the PTFE insert is indicated by //. E_f and Δ_{clamp} are he flexure modulus and clamping correction determined according to ISO-15114 [3].

Table 2
Engineering constants of DT120 carbon/epoxy prepreg [34].

E_{11} (GPa)	E_{22} (GPa)	E_{33} (GPa)	G_{12} (GPa)	G_{13} (GPa)	G_{23} (GPa)	υ_{12}	υ_{13}	υ_{23}
145.0	6.4	6.4	3.38	3.38	3.92	0.26	0.26	0.31

effect of stiffness on mode II delamination behaviour is not yet well understood.

Therefore, this study aims to examine the discrepancies and consistencies between UD and MD laminates in their mode II delamination behaviours by conducting a series of End-Loaded Split (ELS) tests using specimens with different layups and initial delamination interfaces. Characterizing delamination growth relying on a uniaxial (1-D) crack length is inadequate, particularly when the delamination growth in MD laminates does not have a straight-line front perpendicular to the growth direction [31–33]. Thus, the comparison between MD and UD specimens is grounded on the measurement of delamination area. This was accomplished through 3D Digital Image Correlation (DIC) analysis coupled with an equivalent Strain Energy Density (eSED) method. Various data reduction methods were employed to obtain the fracture resistance of MD and UD specimens. The total Energy Release Rate (ERR) was determined by calculating the total energy dissipation per delamination area based on the force–displacement response, while the ERR corresponding to the actual delamination growth was derived through a modified J-integral method. Through fractographic observations, the mode II delamination mechanisms were discerned. Subsequently, the characterization of mode II delamination growth was achieved by decomposing fracture resistance in alignment with the delamination mechanisms identified.

2. Experiment

2.1. Material and specimen configurations

The material system used in the experiments was a unidirectional carbon/epoxy prepreg system, M30SC-150-DT120-34F, manufactured by Delta Tech Italy [34]. UD and MD laminates were designed to investigate the influence of stacking sequences and interfacial properties on mode II delamination behaviour. The specimen details are given in Table 1. For the "UD" specimens, the middle interfaces were designed to be 0°//0°, 0°//90°, and 90°//90°, facilitating comparison with MD laminates featuring identical interfaces.

The specimens were fabricated through manual layup and subsequently cured in an autoclave. The curing cycle followed a technical data sheet provided by the manufacturer [34]. Specimens of identical dimensions, measuring 180 × 20 mm^2, were cut from a cured plate with dimensions of 200 × 200 mm^2 using a Proth automatic cutting machine. Each specimen had a thickness of 2.5 mm, comprising 16 plies. To introduce an initial 55 mm delamination (a_0 = 55 mm), a 16 μm thick Teflon insert was positioned at the central interface before curing, spanning the width of the plate. The engineering constants of the material system are given in Table 2.

2.2. Test setup and procedure

Following the ISO-15114 test standard, an ELS test setup was utilized in the experimental campaign to determine the mode II fracture resistance. The ELS test setup has the advantage of providing a stable mode II delamination growth, compared to End Notch Flexure (ENF) or 4-point bending tests [3,35,36]. As shown in Fig. 1a, a Zwick testing machine with a 1kN load cell was employed. The loading block was glued to the specimen and connected to an fixture with a pin constraint (Fig. 1c). The 1kN load cell was bolted to cross head with an extended cylindrical bar. The length of the cylindrical bar was 800 mm, providing ample space for 3D DIC cameras equipped with a 25 mm lens. The specimen was fully clamped with two pieces of sliding blocks. The torque applied to the bolts was fixed at 5 N·m for clamping the specimen. A thin layer of white ink with markers of 1 mm increment was applied to the edge of the specimen in order to measure delamination growth at one side (Fig. 1d). A travelling microscope was placed on the other side to capture delamination migration and fibre bridging.

As shown in Fig. 1(b), 3D DIC analysis was performed using a VIC-3D system (Correlated Solutions, Inc.). The angle between the two cameras was 20° and the working distance of the cameras was 600 mm. The speckle pattern for DIC analysis was carefully painted on the top surface with a speckle size of approximately 3 pixels. The frames used to fix the cameras were constrained on the moving bed alongside the ELS fixture, ensuring that the cameras remained focused on the top surface.

In addition, an acoustic emission (AE) sensor (Vallen System, VS900-M) was attached to the end of the specimen, outside of the clamping region, in order to detect initiation of delamination growth. The sampling rate for AE recording was 10 MHz, with a threshold of 40 dB determined based on preliminary testing.

The specimens were pre-cracked to 5~10 mm under mode II loading, following the recommended pre-cracking method in the standard [3]. The specimen was clamped with a free length of $L_0 = a_0 \times (4 \times 3) = 45 \times (4 \times 3) = 60$ mm for pre-cracking. Pre-cracking was halted upon an instantaneous drop in force, indicating that the initial delamination had propagated near the clamping edge. The initial insert was 45 mm, extending to approximately 55 mm after pre-cracking for all specimens. A summary of the specimen geometry after pre-cracking is provided in Table 1. The test was performed under displacement control with a loading rate of 1 mm/min for both pre-cracking and formal testing. At least three specimens were tested for each configuration. After testing, a remote mode I loading with a 4 mm opening displacement was applied to the specimens to observe fibre bridging at the interfaces.

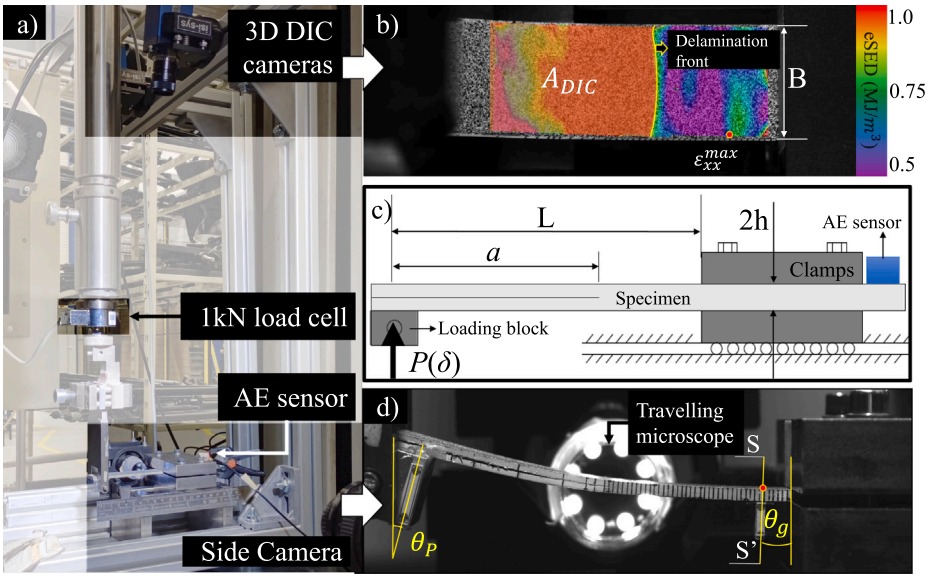

Fig. 1. (a) Experiment setup, (b) DIC calculated eSED field, (c) illustration of test configuration, (d) image for measurement of edge delamination and specimen rotation.

2.3. DIC-eSED method for delamination area measurements

Since delamination growth is essentially multi-directional, the delamination front may not always be perpendicular to the growth direction [37,38]. Thus, this study proposes a method to track and measure delamination growth throughout the loading process by integrating 3D DIC analysis with an equivalent Strain Energy Density (eSED) approach. The eSED was calculated as follows:

$$S^{equ} = \frac{1}{2}(\sigma_{xx}\varepsilon_{xx} + \sigma_{yy}\varepsilon_{yy} + 2\sigma_{xy}\varepsilon_{xy}) \tag{1}$$

where the strain components ε_{ij} $(i,j = x,y)$ were obtained from DIC analysis. The derivation of Eq. (1), detailed in Appendix, is based on Classical Laminate Theory (CLT).

The eSED field is illustrated in Fig. 1(b). A high eSED gradient can be recognized at the vicinity of an estimated delamination front. This is mainly attributed to additional bending moments experienced by the upper and lower sublaminates at the delamination front. A clearer separation between the delaminated and intact regions can be identified by applying a threshold range (0.68 MJ/m^2 to 1.00 MJ/m^2) to the eSED field, as depicted in Fig. 2 (II). This threshold was determined by trial and error until the eSED gradient narrowed down to the delamination front at different stage of delamination growth for various specimen configurations. The extension of the delamination area for each measurement point ΔA_i is determined by subtracting the current area with the initial delamination area A_0. The measurement was comparable to the edge measurement of delamination length multiplied by the specimen width, $a \times B$ (Fig. 6).

The longitudinal strain field (Figs. 2(a) and 2(b) (I)) can serve as an additional method to track delamination growth. Nonetheless, the delamination front appears ambiguous, and the strain values vary across different specimen configurations.

2.4. Data reduction methods

Three different methods are recommended in the test standard for determination of fracture toughness [3]: Simple Beam Theory (SBT), Experimental Compliance Method (ECM), and Corrected Beam Theory using Effective crack length (CBTE). The calculation of G_{IIc} is based on the Irwin–Kies formula:

$$G_{IIc} = \frac{P^2}{2B} \cdot \frac{dC}{da} \tag{2}$$

where C is the compliance. The ECM and SBT methods are based on the experimental measured crack length at the edge, while CBTE method calculates an effective crack length in accordance with the variation of compliance induced by crack growth:

$$a_e = \left[\frac{1}{3}\left\{2bCh^3E_f - (L + \Delta_{clamp})^3\right\}\right]^{1/3} \tag{3}$$

where E_f and Δ_{clamp} are the flexural modulus and clamping correction. For UD laminates, the CBTE method demonstrates the highest level of reproducibility and is recommended to adhere to by the standard [3, 39]. The experimental flexure modulus and the clamping correlation are given in Table 1.

The standard methods are based on Linear Elastic Fracture Mechanics (LEFM) where the Fracture Process Zone (FPZ) is assumed to be small in comparison with the dimension of the specimen. However, mode II delamination growth in MD laminates involves a large FPZ due to the shear-induced matrix cracks ahead of the delamination front [40–43]. In such cases, the J-integral method offers a better solution for characterizing non-linear fracture behaviour. The fundamental form of the J-integral can be expressed as:

$$J = \int_{\Gamma}\left[\omega dz - T_k\frac{\partial u_k}{\partial x}ds\right](k = 1,2) \tag{4}$$

where Γ is the contour for the integral, ω is the strain energy density, x and z are the horizontal and vertical coordinates, T_k is the traction force, u_k is the displacement vector, ds is the infinitesimal arc length along Γ.

For the ELS test, a closed-form solution incorporating large deformation correction was proposed by Pérez-Galmés et al. [40] as follows:

$$J = \frac{P(\cos\theta_P)}{b}\tan(\theta_P - \theta_g) + \sum_{k=1}^{n}\int_{-h_k}^{h_k}\left(-\frac{1}{2}\sigma_{xx}\varepsilon_{yy} + \sigma_{xz}(\varepsilon_{xz} - \tan\theta_g)\right)dz \tag{5}$$

The second term in the contour integral indicates the strain energy due to bending deformation at section S-S' in Fig. 1d. Two rotation angles, θ_P and θ_g, are measured from images captured by the side camera, as depicted in Fig. 1(d). The longitudinal strain ε_{xx} distribution through the thickness is assumed to be linear with ε_{xx}^{max} determined from DIC analysis. The shear strain ε_{xz} was approximated using a parabolic shear strain distribution along the thickness:

$$\varepsilon_{xz} = \frac{3P(\cos\theta_P)(h^2 - z^2)}{4bh^3G_{xz}} \tag{6}$$

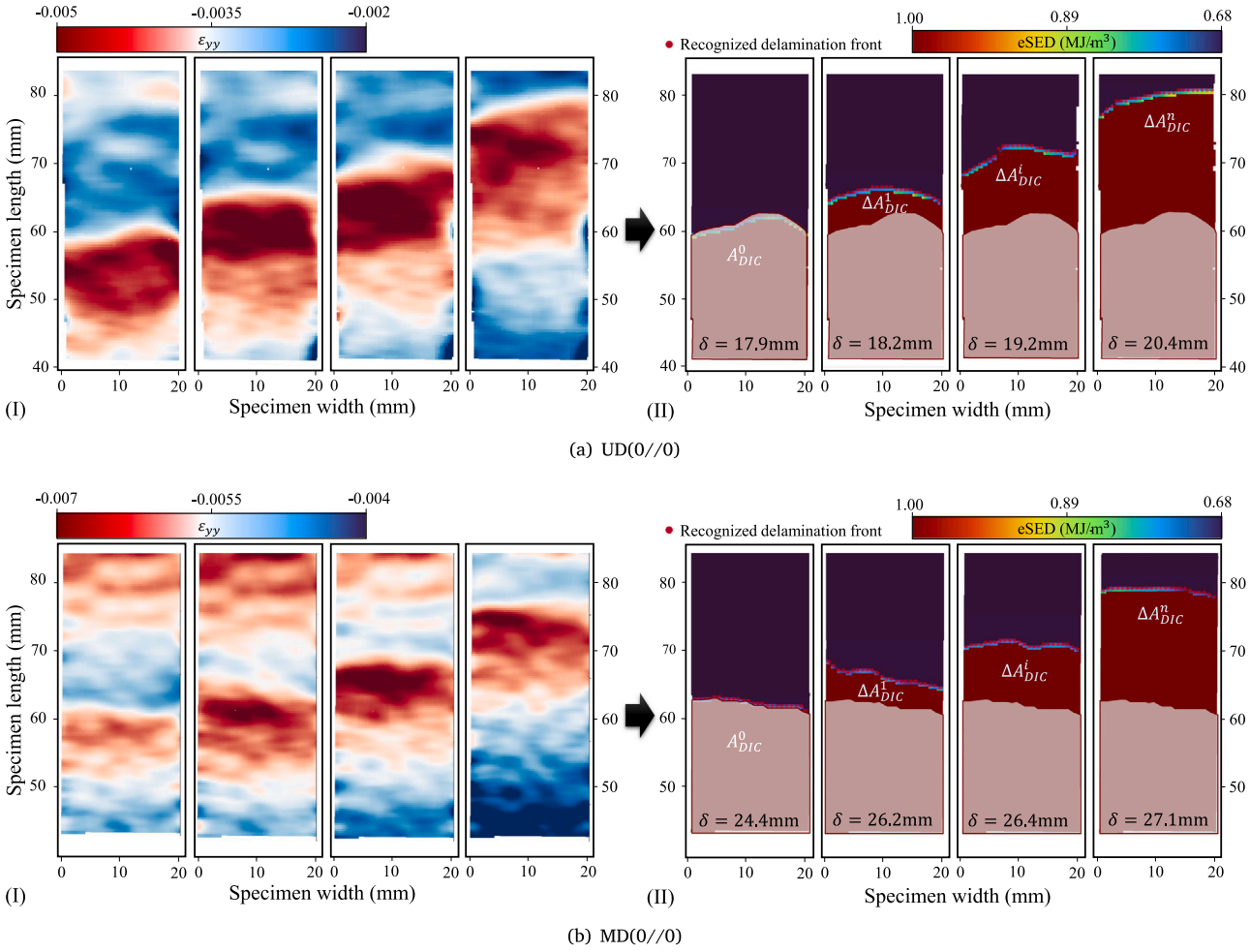

Fig. 2. Monitoring delamination growth by implementing DIC-eSED method for (a) UD(0//0) and (b) MD(0//0) specimens. (I) Longitudinal strain ε_{yy} field at different delamination stages. (II) Calculated eSED field with recognized delamination front denoted by red dots. The area (dark red) below the delamination front is the fully delaminated region. Delamination growth of the ith measurement $\Delta A^i_{DIC} = A^i_{DIC} - A^0_{DIC} (i = 1, 2, \ldots, n)$. A^0_{DIC} is the initial delamination area after pre-cracking. (For interpretation of the references to colour in this figure legend, the reader is referred to the web version of this article.)

For MD laminates, the stress components can be calculated using CLT, enabling the solution of the J-integral.

Furthermore, a physical ERR method was employed to obtain the total G^{tot}_{IIc}, involving all forms of energy dissipation and toughening mechanisms. The calculation of the physical ERR relies on measuring the increment in delamination area dA_i and extracting the corresponding energy dissipation. This method, referred to as the AREA method, has been described in previous works such as Refs. [40,41,44,45].

$$G^{tot}_{IIc} = \frac{dU}{dA} \tag{7}$$

The fracture resistance G_{IIc} derived using different data reduction methods is compared in the following sections.

3. Experimental results

3.1. Delamination growth and physical ERR

Representative force–displacement curves from the ELS tests are shown in Fig. 3. The measurement points for the increment of delamination growth are illustrated and denoted by da^i and dA^i_{DIC}. For every increment, the relevant energy dissipation dU is calculated by the shaded grey area [44]. For MD laminates, a non-linear force–displacement behaviour is presented due to large displacement and friction at the sliding fixture during loading process. The calculation of dU was based on the. This was validated by performing multiple loading and reloading steps on a group of MD specimens, as shown in Fig. 3(b). A fourth order polynomial fit, incorporating a shifted nonlinear part (highlighted in blue in the first loading curve) and an additional point at the origin, can be performed to obtain the reloading force–displacement curves. The shifting distance was determined by the difference in displacement between the measurement point and the corresponding point with the same force in the first loading curve.

Based on Eq. (7) and assuming a constant physical ERR throughout the delamination process, the physical ERR can be acquired from the slope of a linear fitting dA_{DIC} - dU or da×B - dU plot. The delamination area calculated using da×B is based on the assumption that the delamination front is straight and normal to the growth direction. However, as shown in Fig. 2, a curved delamination front can be observed in reality. The fitting curve with the dA_{DIC} demonstrates reduced scatter and a higher Coefficient of Determination (COD) since

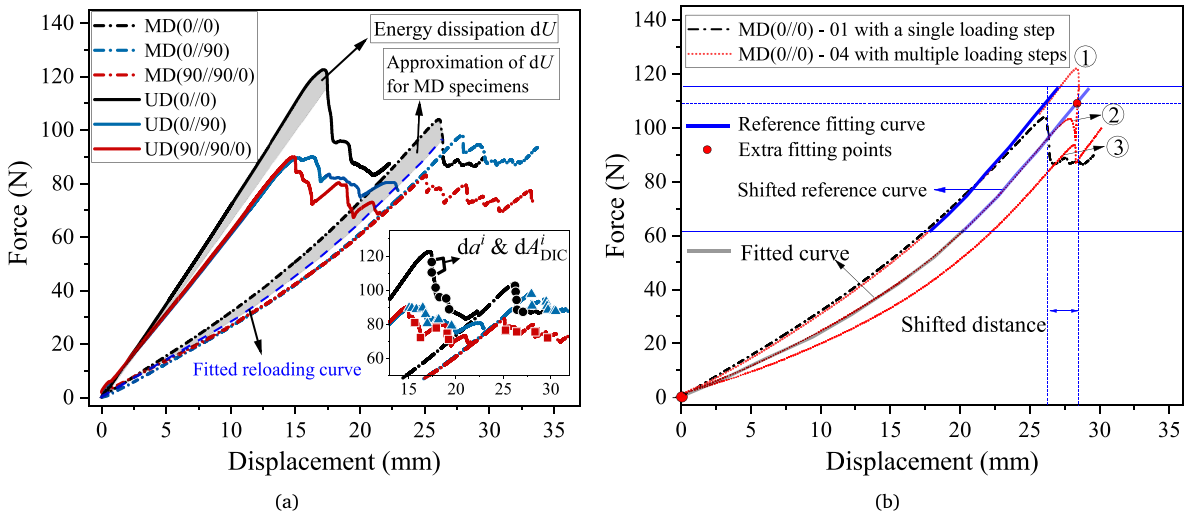

Fig. 3. (a) Force–displacement behaviours and measurement points of the increments of delamination growth da_i dA^i_{DIC} and the corresponding energy dissipation dU. (b) Example of the curve fitting for reloading curves of MD specimens. (For interpretation of the references to colour in this figure legend, the reader is referred to the web version of this article.)

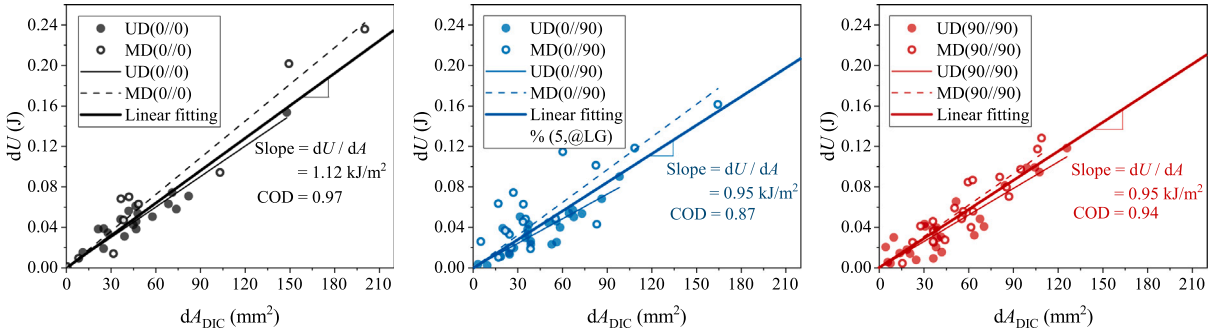

Fig. 4. Calculation of the physical ERR using the measurement of increments of delamination area dA_{DIC}. The slope of the linear fitting through the thick solid line indicates the physical ERR of MD and UD specimens with identical interfaces.

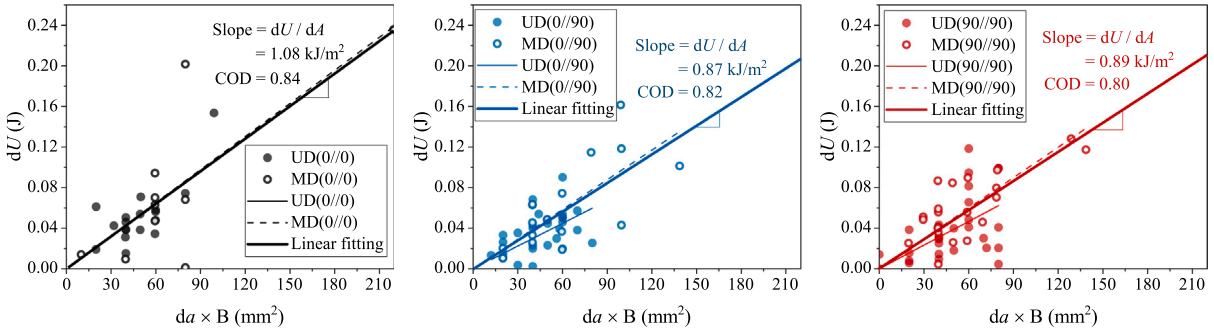

Fig. 5. Calculation of the physical ERR using the measurement of increments of delamination length da×B.

the actual delamination area can be determined, as shown in Figs. 4 and 5. Furthermore, using different measurement methods, similar trends of delamination growth are presented in Fig. 6. Mode II delamination growth initiated towards the latter stages of the loading process, exhibiting a rapid growth within a limited range of displacement loading. Delamination growth occurred within a small displacement range. The 0°//0° interface presents a more instant propagation process compared to the others. In UD specimens, the growth curves of 0°//90° and 90°//90° interfaces nearly aligned with each other. For the 90°//90° interface, the initial delamination migrated to an upper 90°//0° interface and propagated along the 0° ply as shown in Fig. 10(II) (c) and (f). Migration triggered fibre band bridging at the affected location, leading to delamination growth at higher force and displacement compared to MD(0//90). Nevertheless, the trends between 0°//90° and 90°//90° interfaces exhibit similarities.

The area measurement through DIC-eSED method provided a more accurate characterization of delamination growth in terms of determination of the physical ERR and quantitative analysis of the delamination behaviour. Therefore, the area measurement using the DIC-eSED method was used to derive the R-curves.

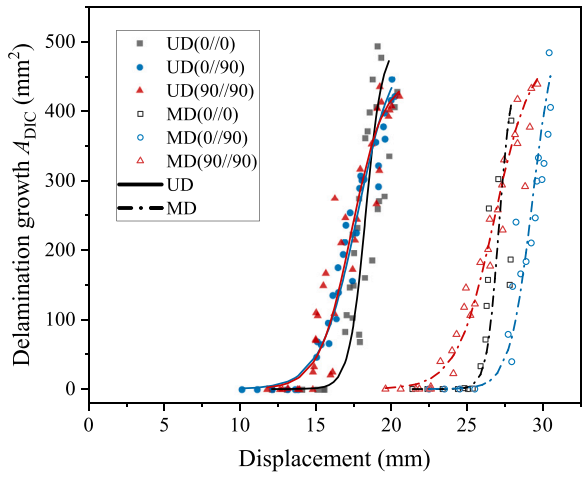

(a) DIC-eSED measurement

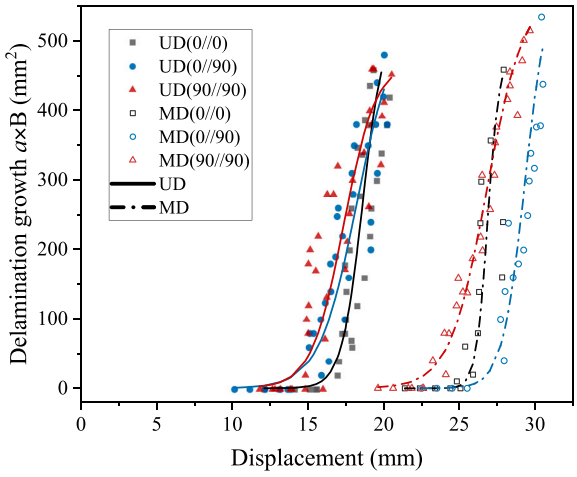

(b) Edge measurement

Fig. 6. Measurement of delamination growth with different methods..

3.2. R-curves

To derive the R-curves, ISO-15114 recommends three distinct methods for determining the initiation point of delamination growth: visual determination of initiation point (VIS), initiation of non-linear force–displacement response based on initial compliance (NL); 5% decrease in the compliance compared to the initial compliance ($C_{5\%}$). Given the pronounced non-linear behaviour observed in the force–displacement profiles of MD specimens, both the VIS and NL methods prove inadequate for determining the initiation of delamination. Therefore, an Acoustic Emission (AE) technique was employed to determine the initiation point, relying on the variations in the sentry function [46–48]. The sentry function is defined as the logarithm of the ratio of mechanical energy to acoustic energy [49,50]:

$$f_s(x) = Ln\left[\frac{E_S(x)}{E_a(x)}\right] \tag{8}$$

The mechanical energy $E_S(x)$ is calculated as the area under the force–displacement curve at a displacement level x, while the $E_a(x)$ is the cumulative acoustic energy of the AE events at the same displacement level.

As shown in Fig. 7, the sentry function curves can be separated into three distinct phases. Unstable oscillation in the sentry curves can be observed at phase I. Different specimens have shown distinct trends in the sentry curves at the early stage. This is mainly attributed to different interface conditions after pre-cracking. Depending on the specimen interfaces, the fewer acoustic events, which are mainly caused by the interface friction during phase I, show differences in term of quantity, amplitude and energy, which affects the sentry curves. When the acoustic energy generated by AE events increases, a decline in the sentry curves can be observed. Subsequently, phase II exhibits a gradual rise in the sentry function, indicating a stable increase in the mechanical energy and acoustic energy during loading. In phase III, a noticeable slope change in the sentry function indicates the initiation and propagation of delamination that generated AE events with higher energy and amplitude. The transition between phase II and phase III is regarded as the initiation point of delamination growth.

Having identified the initiation point, the fracture resistance was computed using the J-integral. As shown in Fig. 8, a boundary delineating unstable and stable delamination growth can be discerned (indicated by the vertical dashed lines where the slope of the R-curve approaches zero). The increase in the R-curve is mainly attributed to the development of FPZ and coalescence of micro matrix cracks that form the delamination surface [41,43,51]. As delamination propagates, various damage mechanisms gradually activate, including fibre–matrix debonding and fibre breakage (Fig. 11). Compared to UD specimens, MD specimens exhibit a higher increase in the R-curve and a longer range of delamination growth that involves FPZ development. Eventually, the ERR stabilizes once the formation of new delamination and FPZ stabilizes, signifying a stage where unit delamination growth releases the same amount of energy due to consistent damage modes. The fracture resistance close to the initiation of delamination growth was lower than that observed during the stable propagation stage, suggesting the inception of micro-matrix cracking ahead of the crack tip.

For all specimen configurations, the physical ERR (indicated by the horizontal dashed lines) is higher than the ERR calculated using J-integral. Especially for the ERR of stable delamination growth in 0°//0° specimens.

For UD specimens, data reduction methods suggested by ISO-15114 were employed to determine G_{IIc}. As shown in Fig. 9, the comparison of G_{IIc} results obtained through different methods is presented. For 0°//90° and 90°//90° interface, the discrepancies between the G_{IIc} values derived from standard methods, AREA method, and J-integral are relatively smaller, in contrast to the 0°//0° interface. A notable disparity exists between the G_{IIc} obtained from J-integral and the physical ERR for 0°//0° interface. This discrepancy arises because the J-integral method calculates the energy dissipation attributed to solely delamination growth [40], whereas the other methods incorporate both intrinsic energy dissipation due to delamination growth and extrinsic toughening effects, such as friction, fibre bridging and geometric nonlinearity (in MD specimens), in determining G_{IIc}.

3.3. Mode II delamination mechanisms

In order to investigate the effect of fibre bridging on mode II delamination growth, a mode I opening load was applied to the specimen after testing, as illustrated in Fig. 10. The fully delaminated region Ω, measuring 20 × 20 mm^2, was cut from the specimen and used for fracture texture analysis using a 3D optical profilometer (Keyence VR-5000) and fractography with a Scanning Electron Microscope (SEM, JSM-7500F).

The observation at section F-F' was performed by using the travelling microscope (Fig. 1(d)). As shown in Fig. 10(I), a substantial quantity of bridging fibres was observed at the 0°//0° interface in both MD and UD specimens (Fig. 10(II) (a) and (d)). At the 0°//90° and

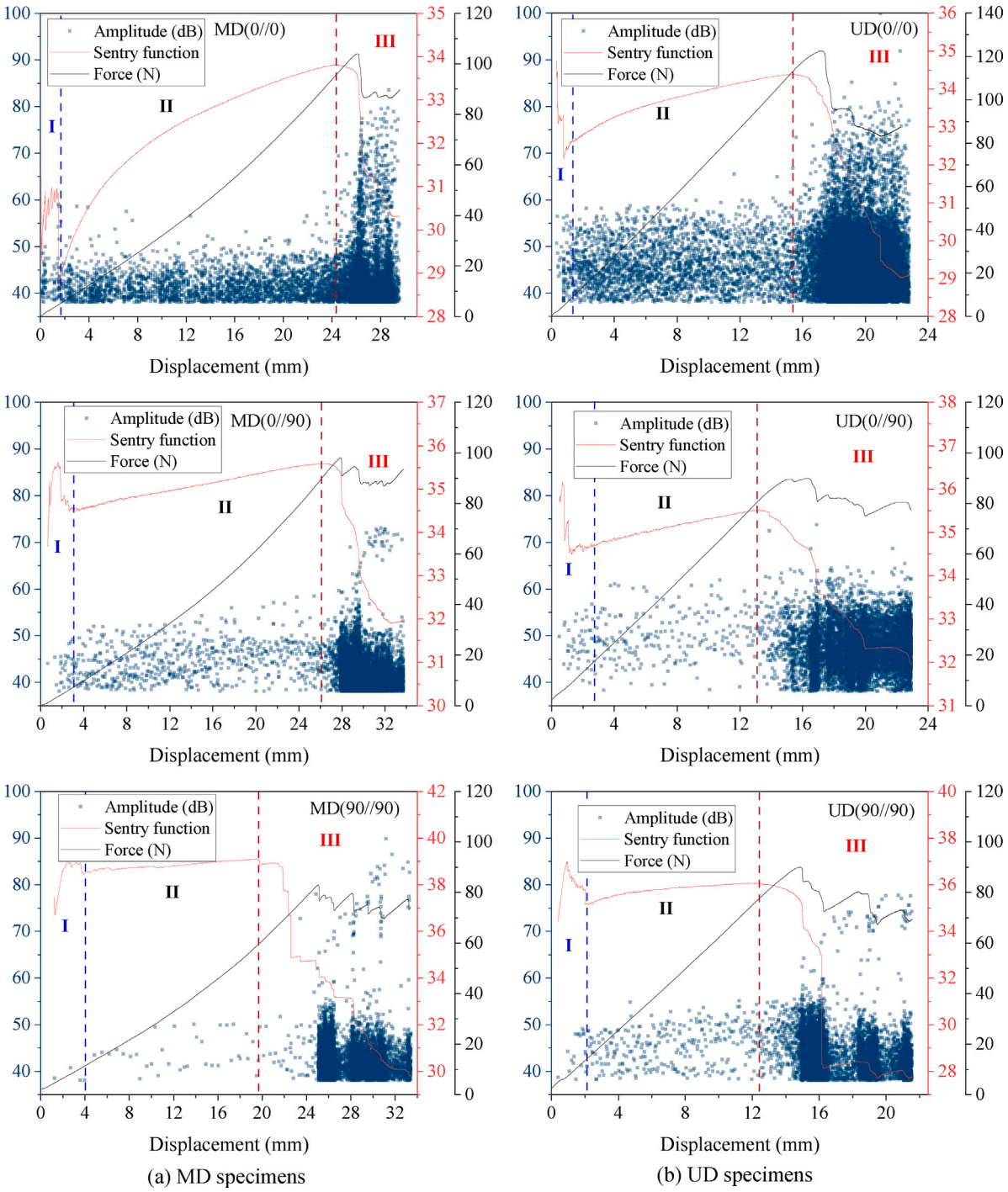

Fig. 7. Determination of initiation points for different specimen configurations using the sentry function.

90°//90° interfaces, fibre bridging was solely evident in MD laminates. Delamination migration occurred at the initial 90°//90° interface, followed by propagation of the migrated delamination at an upper 0°//90° interface. The migrated delamination interface (Fig. 10(II) (f)) exhibited a fibre bridging pattern similar to that observed at the middle 0°//90° interface (Fig. 10(II) (e)). The bridging angle θ_{fb} at 0°//0° interface is larger than that of the 0°//90° interface, resulting in a shorter bridging distance and thus more bridging fibres within the same delamination area. In addition, intralaminar cracking occurred in the 90° layer of UD specimen with 0°//90° interface, likely due to larger shearing in the 90° layer, as the other 0° layers are more resistant to shearing.

The bridging fibres started near the pre-crack and sustained throughout the entire delamination process. This resulted in a bridging zone that extended across nearly the entire delamination region. Especially for 0°//0° interfaces, the large-scale fibre bridging promotes a more significant toughening effect. The presence of bridging effects facilitated additional energy dissipation through fibre pullout, fibre–matrix debonding, and potential fibre breakage. This accounts for the higher physical ERR compared to the ERR calculated using the J-integral method as shown in Fig. 8. As for the 0°//90° interface, the ERR calculated by various methods closely aligns, indicating an insignificant bridging effect. Compared to the 0°//0° interface, the higher ERR for stable delamination growth at the 0°//90° interface, as calculated by

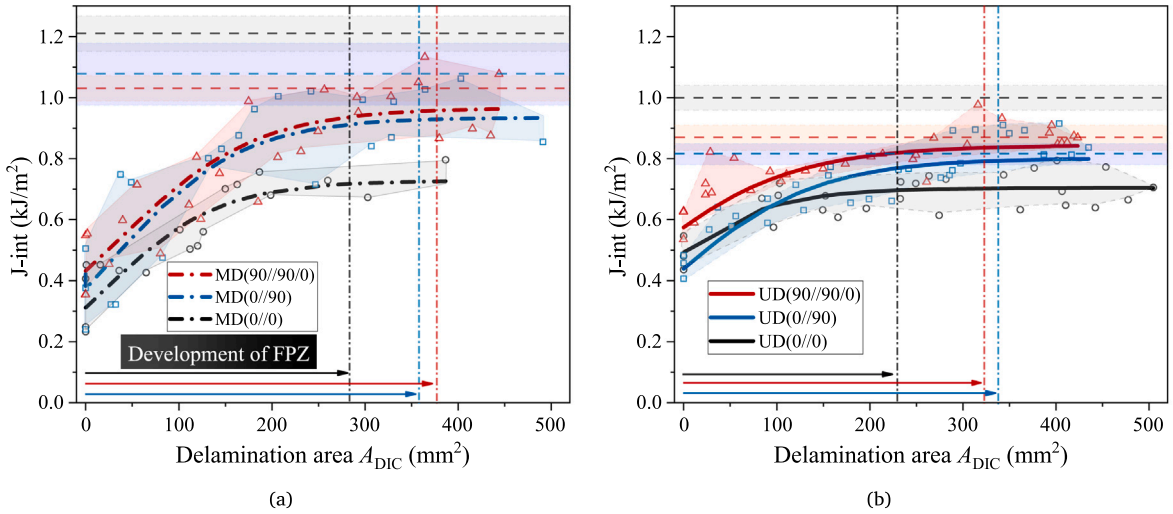

Fig. 8. Experimental R-curves of all specimen configurations: (a) MD layup, and (b) UD layup. The master curve was obtained by using a logistic fitting function, and the area underneath covers all the scatter points for each specimen configuration. The parallel dashed lines indicate the physical ERR, and the area around them is the 95% confidence interval of the slope from the linear fitting of dU/dA_{DIC}.

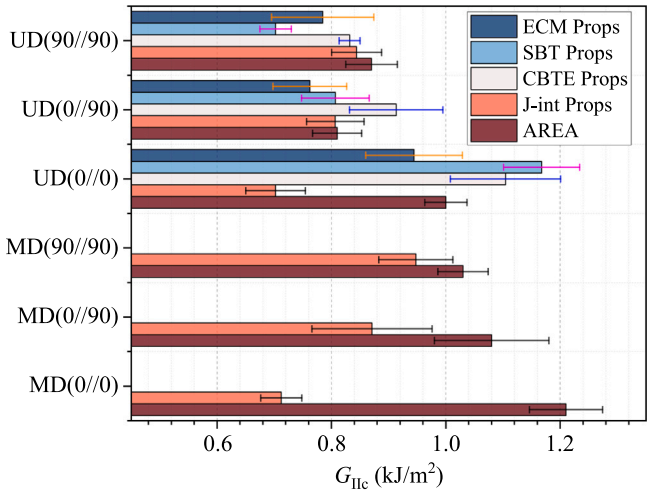

Fig. 9. Comparison of G_{IIc} determined by different measurement methods. Props indicates the mean G_{IIc} calculated from all points at stable delamination growth stage. The error bars indicate the 95% confidence interval for the determination of G_{IIc} using the AREA method, and the standard deviation for determination of G_{IIc} using the other methods.

the J-integral method, can be primarily attributed to differences in interface texture.

As illustrated in Fig. 10(I), the main cause of the large-scale fibre bridging at the 0°//0° interface in both MD and UD laminates is attributed to the nesting of 0° fibres. This phenomenon arises due to the compression of the 0° fibres into the adjacent layer during the curing process, a phenomenon exacerbated by the UD layup, as illustrated in Fig. 10(I) (a). As for 0°//90° interfaces in Fig. 10(I) (b), (c), (e) and (f), the red colour indicates the delaminated resin-rich region within the 90° ply.

Fractography using SEM provides a clearer observation of the matrix cracks. As shown in Fig. 11, dense micro matrix cracks (cusps [20, 52,53]), along with fibre pull out, can be identified at the 0°//0° interfaces for both MD and UD specimens. For 0°//90° interface, large-area matrix cracking in the 90° layer was presented. The formation of such extensive matrix cracking can be mainly ascribed to the advancement of matrix cracking within the resin-rich region at the 0°//90° interface. Another notable characteristic of the 0°//90° fracture surface is the presence of large cusps, predominantly resulting from the uneven distribution of 0° fibres along the transverse direction. At the 0°//0° interface, this uneven distribution induces fibre nesting, leading to more bridging fibres.

As shown in Fig. 10, cutting plane C–C' was used to investigate the FPZ of all specimens, minimizing edge effects. The microscopic views of section C–C' are presented in Fig. 13 and Fig. 14. A comparison between the fully delaminated interface and the intact interface is also provided in Fig. 12. The observation was conducted with a 1 mm opening, approximately 20 mm behind the crack tip, to provide clearer identification of the crack tip. For specimens with 0°//0° interface, the FPZ lengths of MD and UD specimens were similar, leading to closely matched G_{IIc}^{prop} values by J-integral (Fig. 8). Compared to MD specimens, UD specimens with 0°//90° interface presented a longer FPZ. This can be attributed to a longer high-stress region in the shear stress profile along the specimen length due to the higher stiffness of UD specimens [29]. However, the UD specimens show a lower G_{IIc}^{prop} value compared to MD specimens. This can be attributed to an elevated shearing effect in the 90° layer, as the stiffer 0° layers transfer higher shear force to the middle 90° layer.

4. Characterization of mode II delamination growth

4.1. Effects of fibre bridging and specimen stiffness on fracture toughness

As shown in Fig. 9, MD specimens presented a higher G_{IIc} than UD specimens, as determined by the AREA method. This can be mainly attributed to the effect of geometric nonlinearity [55] (large displacement) on the force–displacement response, which directly affects the calculation of dU in MD specimens with lower stiffness (Figs. 3 and 4).

As shown in Fig. 8, MD specimens exhibit a large gap between the determined crack initiation and the stable propagation stage, as well as a longer range of FPZ development compared to UD specimens. This indicates a slower saturation of dominant fracture mechanisms occurring during stable delamination growth. For delamination initiation, the lower G_{IIc} values in MD specimens can be attributed to the smoother delamination surfaces, as illustrated in Fig. 10. For stable growth, a constant G_{IIc} is achieved when the crack opening is sufficiently large to break the bridging fibre bundle in mode I [29]. In mode II, however, the bridging fibres span the entire delamination interface, indicating that the bridging traction [56] is present across the interface throughout

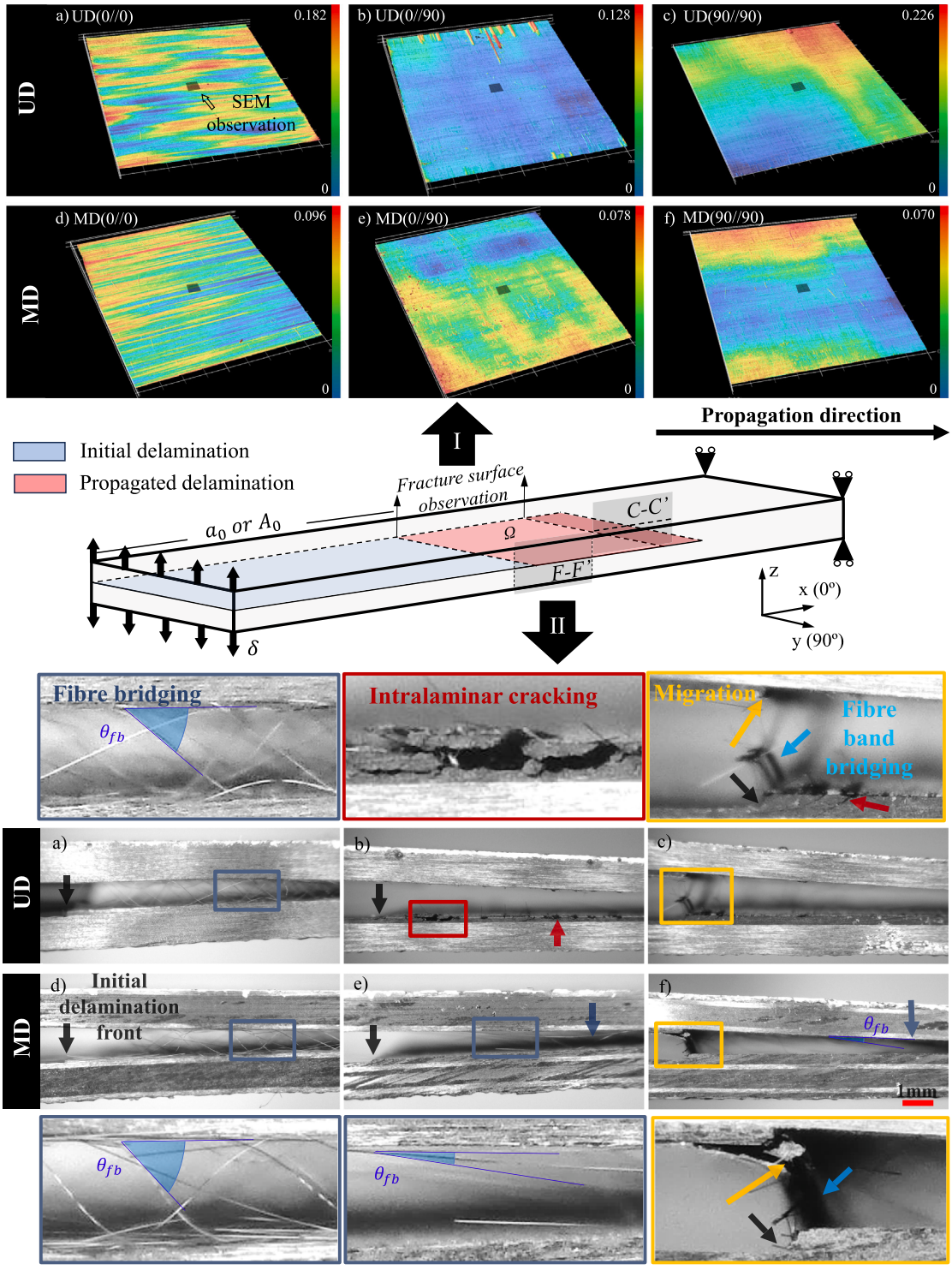

Fig. 10. (I) Fractographic observation at the fracture surface of the upper sub-laminate Ω, and (II) observation of fibre bridging at side section $F - F'$.

the duration of the test. The plateau in the R-curves of MD and UD specimens with 0°//0° interface may indicate stable growth, where the length of pullout fibres stabilizes. In addition, the bridging fibres at 0°//0° interface are shorter than those at 0°//90° interface in MD specimens. This can lead to delayed stable growth for 0°//90° interfaces, resulting a longer FPZ development, as fibre-matrix debonding and fibre pullout persist during extended delamination growth. As for UD specimens with 0°//90° interface, where there is no fibre bridging, the increase in the R-curves can be attributed to the evolution of FPZ ahead of the crack tip.

The stiffness of the specimen may influence the development of both the fibre bridging zone behind the delamination front and the FPZ ahead of it, thereby affecting the fracture toughness. As shown in Fig. 2, the MD specimen exhibits more localized bending deformation near the crack tip compared to the UD specimen. This can cause a more gradual redistribution of shear stress, necessitating longer delamination growth to stabilize the development of the fibre bridging zone and FPZ Fig. 8.

In this study, the effect of specimen stiffness on the fracture toughness can be mainly attributed to geometric nonlinearity. By designing a stiffer MD specimen with additional layers or a different layup, the

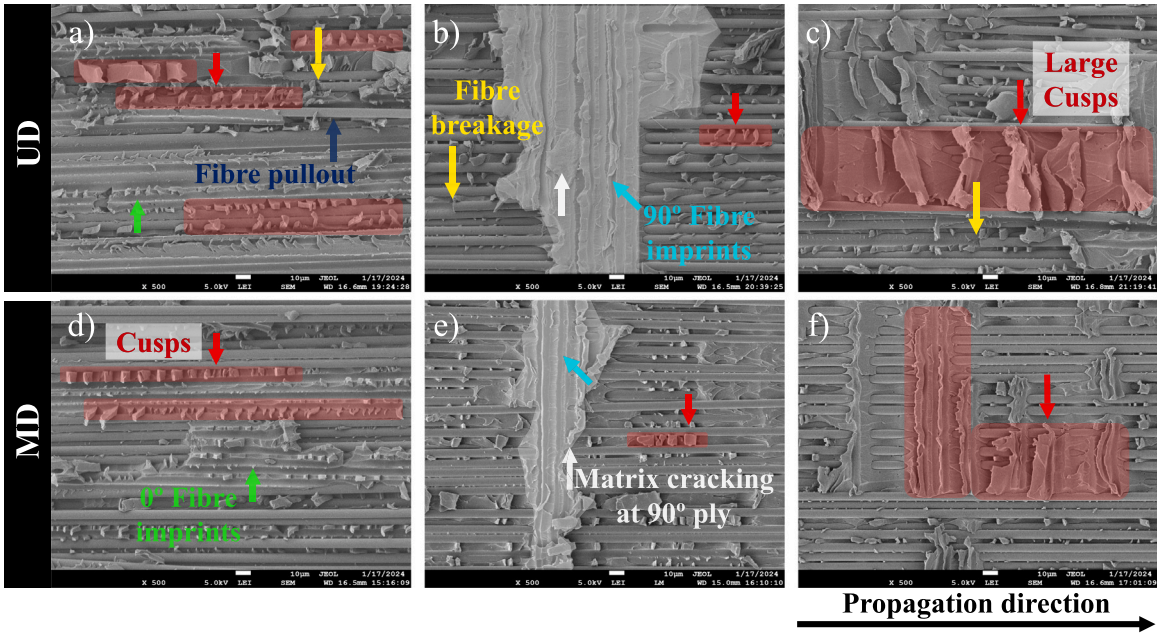

Fig. 11. Fractographic observation at the upper delaminated surfaces using SEM, (a) UD(0//0), (b) UD(0//90), (c) UD(90//90), (d) MD(0//0), (e) MD(0//90), (f) MD(90//90).

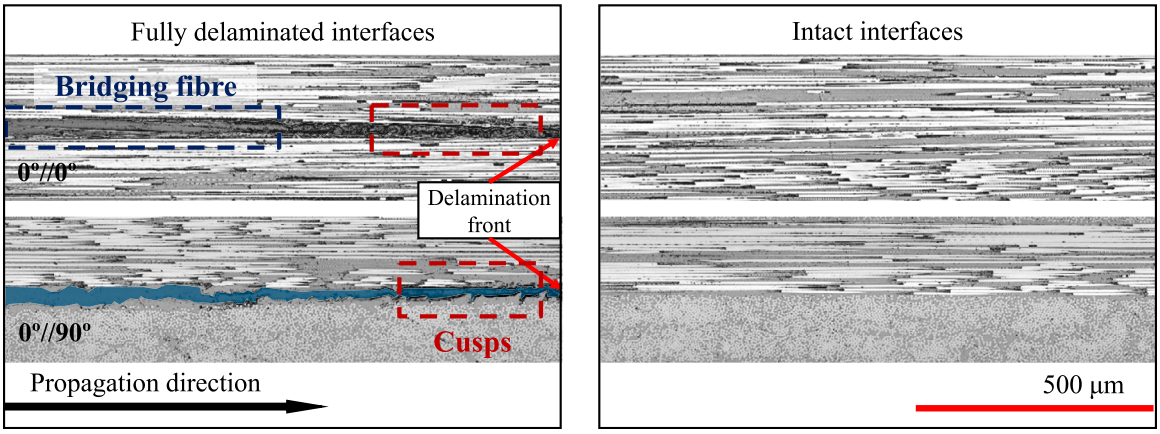

Fig. 12. Comparison between fully delaminated and intact interfaces in specimens with different configurations.

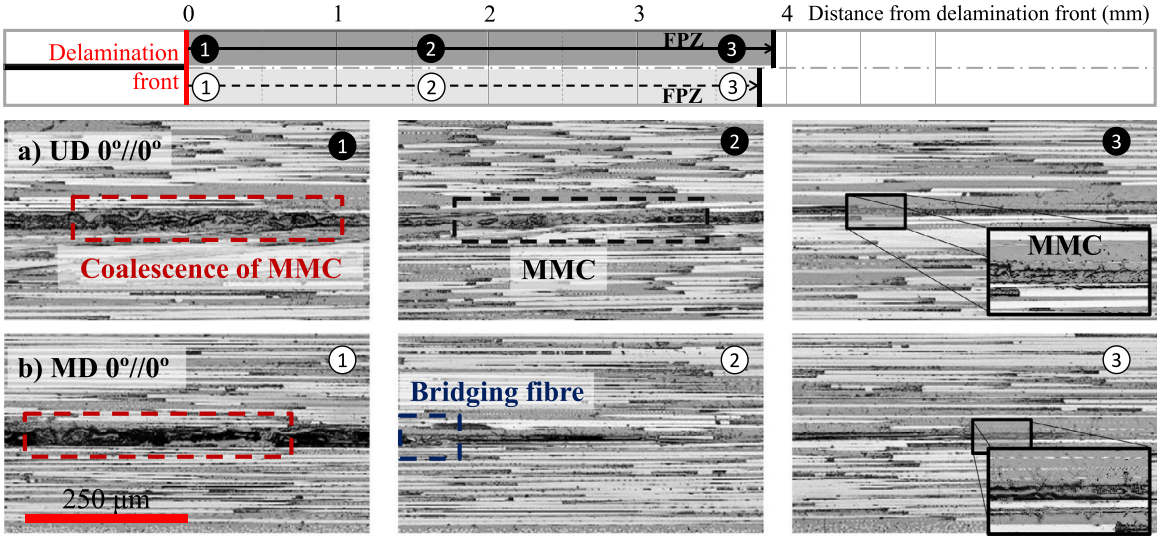

Fig. 13. Observation of the FPZ ahead of the delamination front in UD and MD specimens with a 0°//0° interface. MMC indicates micro matrix cracking. The determination of the FPZ was based on the definition mentioned in Ref. [54], where the coalescence of MMC was still in progress.

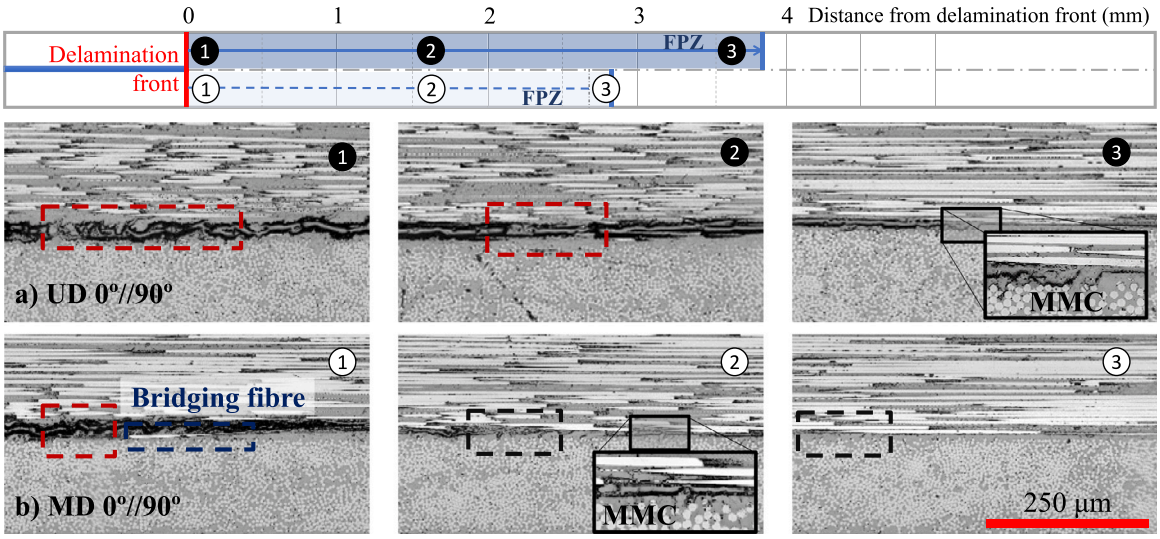

Fig. 14. Observation of the FPZ ahead of the delamination front in UD and MD specimens with a 0°//90° interface.

geometric nonlinearity (large displacement) can be mitigated. This may lead to different outcomes in the comparison of fracture toughness between MD and UD specimens. Further investigation is needed using analytical or numerical tools to enhance the understanding of how specimen stiffness affects the formation of fibre bridging and FPZ development during mode II delamination growth.

4.2. Decomposition of G_{IIc}

The data reduction methods employed for calculating fracture resistance encompass distinct delamination mechanisms, which either consider solely internal effects or incorporate both intrinsic and extrinsic factors. The principle of energy conservation in the ELS test can be formulated as follows:

$$W_{bending} + W_{tensile} = U_e + U_{fb} + U \tag{9}$$

where $W_{bending}$ and $W_{tensile}$ are the external work provided by the bending and tensile force according to the decomposition from Ref. [40], U_e and U_{fb} are the elastic energy storage in the elastic body and the bridging fibres, U is the total energy dissipation and can be further decomposed as:

$$U = U_{mmc} + U_{delam} + U_{fric} \tag{10}$$

where U_{mmc}, U_{delam} and U_{fric} represent distinct forms of energy dissipation attributed to micro matrix cracking ahead of the crack tip, coalescence of the matrix cracks, and friction-related energy dissipation, respectively.

The calculation of G_{IIc} by J-integral omitted contributions from $W_{tensile}$, U_{fb} and U_{fric}. Thus, the ERR was mainly derived from the energy dissipation associated with the formation of the actual delamination area. The initiation G_{IIc} determined by AE was attributed to the formation of matrix cracking at the vicinity of delamination front, whereas the mean value of propagation G_{IIc} signifies the stable delamination growth, driven by the coalescence of the matrix cracks and the development of FPZ where various damage mechanisms were activated. In contrast, the physical ERR calculated by the AREA method includes all energy components outlined in Eq. (9). Therefore, it was the total G_{IIc} for the specific ELS test configuration and material system used in this study.

The total G_{IIc}^{tot} can be decomposed into three components governed by distinct intrinsic damage mechanisms and extrinsic toughening effects [57,58]:

$$G_{IIc}^{tot} = G_{IIc}^{intrinsic} + G_{IIc}^{extrinsic} = (G_{mmc} + G_{delam}) + G_{eff} \tag{11}$$

where G_{mmc} represents the ERR associated with micro matrix cracking at the delamination front, which is equal to the ERR determined by J-integral at the critical initiation point detected by AE $G_{mmc} = J_{int}^{AE}$. G_{delam} is the ERR influenced by other damage mechanisms such as the coalescence of micro matrix cracks, fibre-matrix debonding and fibre breakage, $G_{delam} = J_{int}^{Props} - J_{int}^{AE}$. G_{eff} denotes the effective toughening effect caused by fibre bridging and friction from sliding fixtures $G_{eff} = G_{IIc}^{AREA} - J_{int}^{Props}$. Notably, fibre bridging can be considered as an augmentation of the friction at the delaminated interface, as it does not directly contribute to energy dissipation. Instead, energy dissipation occurs due to further pullout and breakage of the bridging fibres. These are considered as extrinsic toughening effects.

The components of G_{IIc}^{tot} for all specimen configurations are illustrated in Fig. 15, with each components represented as a percentage of G_{IIc}^{tot}. Compared to MD specimens, UD specimens present a higher percentage of ERR for the initiation of delamination growth due to the severe fibre nesting at 0°//0° interface or severe through-thickness matrix cracking at 0°//90° and 90°//90° interfaces (Fig. 10(II)). The various interfaces exhibit disparities in propagation G_{IIc} and total G_{IIc} for both MD and UD specimens. For 0°//0° interfaces, the extensive fibre bridging provides a substantial toughening effect on fracture resistance, leading to a higher proportion of G_{IIc} attributed to extrinsic effects (navy blue area in Fig. 15). For 0°//90° and 90°//90° interfaces, the contribution of extrinsic effects to G_{IIc}^{Props} is due to friction in UD specimens and a combination of fibre bridging, friction and geometric nonlinearity in MD specimens (Fig. 10 (II)). The elevated initiation G_{IIc} for 90°//90° specimens is predominantly associated with fibre band bridging at the migration location.

Given the potential absence of identical extrinsic toughening mechanisms in different structures, relying solely on the physical ERR to predict mode II delamination growth may lead to an underestimation of the delamination progression. This is based on the fact that UD specimens give a lower G_{IIc}^{tot} compared to MD specimens with the same interfaces (Fig. 4). Conversely, utilizing the ERR computed via J-integral may yield an overly conservative prediction by omitting extrinsic toughening effects.

The effects of interface angles on mode II interlaminar toughness of CFRP composites was also investigated by Koord et al. [59]. However, the influence of fibre bridging was not presented. The G_{IIc} of the 0°//0° and 0°//90° interfaces, extracted using the compliance calibration method recommended in ASTM [5], exhibited minimal variation. The highest G_{IIc} was calculated for the 0°//45° interface, likely attributed to its rougher delamination interface. The variance in results between [59] and the current study can be ascribed to the disparities

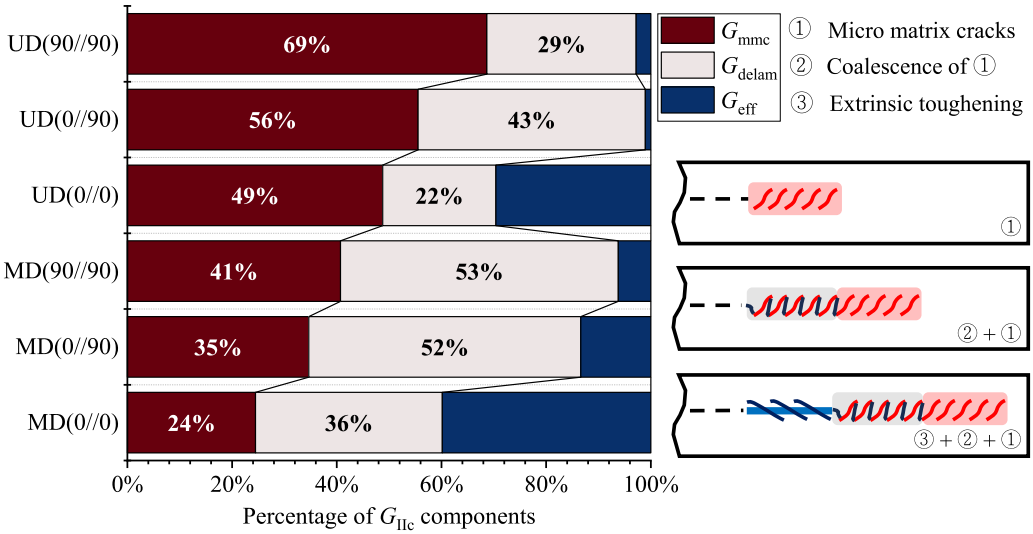

Fig. 15. Proportion of G_{IIc} components of different delamination mechanisms. The percentage indicates the proportion of energy dissipation due to delamination initiation, propagation, and other external effects such as fibre bridging and friction. (For interpretation of the references to colour in this figure legend, the reader is referred to the web version of this article.)

in test configurations (End-Notched Flexure (ENF) and ELS) and the data reduction methods used to derive G_{IIc}. The ELS setup allows a more stable mode II delamination growth [60,61], rendering it ideal for exploring R-curve behaviour in mode II delamination, particularly when combined with the J-integral and DIC-eSED methods presented in this study.

4.3. Monitoring delamination growth with DIC-eSED method

The proposed area measurement method possesses the advantage of mitigating the edge effect and the effect of having a curved delamination front, as it measures the actual delamination area. Furthermore, manual measurement of delamination growth is avoided. By establishing an appropriate eSED threshold, the detection of the delamination front and calculation of delamination area can be automated using a script.

By recognizing the evolving delamination front with a consistent eSED value, a criterion for determination of delamination growth can be established based on the value that is independent of stacking sequences and interface properties. As discussed in Ref. [62], a critical SED required for the initiation of delamination growth remains constant for a specific material system, irrespective of the loading mode. This is because the SED criterion was used to determine the onset of the first micro crack in mode II delamination. In this study, the formation of the successive micro cracks, as shown in Fig. 15, were detected by AE, resulting in a higher ERR for mode II delamination initiation (G_{IIc}^{mmc} = 0.49 kJ/m^2 for UD(0//0)) compared to that extrapolated from the SED method (G_{IIc}^{SED} = 0.20 kJ/m^2 for UD(0//0)) using a similar carbon/epoxy material system. A SED fracture criterion capable of describing the fracture toughness of the material and the direction of crack initiation was outlined in Ref. [63]. The application of the SED criterion is based on the assumption that the fracture energy remains constant across various forms of fracture within a consistent material system. By encompassing all stress components pivotal to crack initiation, the SED presents a critical threshold for crack formation independent to the loading condition.

The fracture toughness determined based on ERR possesses high dependency on both intrinsic and extrinsic factors. The prediction of delamination growth using the physical ERR may result in an underestimation of the delamination progress. On the other hand, using the ERR determined by J-integral may lead to an over conservative prediction since it does not capture the extrinsic toughening. In contrast, the eSED, computed from the surface strain distribution, encapsulates valuable insights into a genuine fracture toughness for delamination growth. Further analytical investigations are warranted to precisely resolve the SED distribution at the delamination front. This endeavour is essential to ascertain the critical SED required for delamination growth.

5. Conclusions

In this study, a series of ELS tests were performed to investigate the effects of laminate stacking sequences and interfaces on the mode II delamination behaviour. A DIC-eSED method was proposed to measure the extension of delamination area throughout the loading process. Based on that, the physical ERR involving all forms of energy dissipation was obtained and compared with the ERR calculated by the J-integral method.

The DIC-eSED method has demonstrated its capacity to yield accurate characterization of mode II delamination behaviour by quantifying the actual delamination area.

The decomposition of G_{IIc}, according to the comparison between the J-integral ERR and physical ERR methods, reveals significant influences of stacking sequence and interface angles on both intrinsic and extrinsic delamination mechanisms. MD and UD specimens with 0°//90° interfaces, including the migrated ones, exhibit higher $G_{IIc}^{intrinsic}$ due to the large-area matrix cracking. Conversely, MD and UD specimens with 0°//0° interfaces show higher $G_{IIc}^{extrinsic}$ attributed to large-scale fibre bridging caused by fibre nesting, thus contributing to higher G_{IIc}^{tot}. Overall, MD specimens with large displacement demonstrate higher G_{IIc}^{tot} compared to UD specimens, primarily influenced by specimen stiffness and interface properties affecting extrinsic toughening mechanisms such as fibre bridging (for 0°//90° interfaces), friction and geometric nonlinearity (for 0°//0° interfaces).

The determination of mode II fracture toughness of CFRP laminates based on solely UD(0//0) specimens is deemed to be insufficient, considering the demonstrated influence of stacking sequence and interface properties on fracture toughness. The J-integral and physical ERR methods extract the lower and upper limits of mode II fracture toughness by excluding or including the extrinsic toughening effects. The eSED method, however, has exhibited potential in providing a consistent fracture criterion solely dependent on the material system. Further refinement of the SED criterion is warranted to establish a robust method for delamination behaviour characterization.

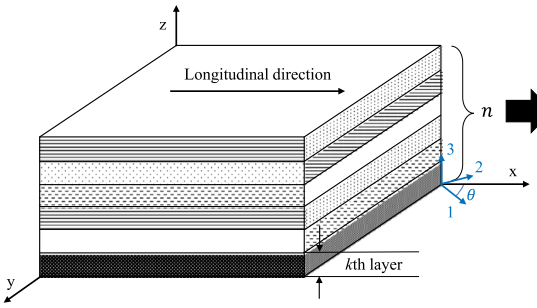

$$E_i^{eqv} = \sum_{k=1}^{n} E_i^k \times \rho^k, i = x, y \quad (20)$$

$$\upsilon_{12/21}^{eqv} = \sum_{k=1}^{n} \upsilon_{12/21}^k \times \rho^k \quad (21)$$

$$\rho^k = \frac{V^k}{V^{tot}}$$

Fig. A.1. Illustration of a MD laminate and the calculation of its equivalent elastic modulus and Poisson's ratio.

CRediT authorship contribution statement

Wenjie Tu: Writing – review & editing, Writing – original draft, Methodology, Investigation, Formal analysis, Data curation, Conceptualization. **John-Alan Pascoe:** Writing – review & editing, Supervision, Resources, Methodology, Conceptualization. **René Alderliesten:** Writing – review & editing, Supervision, Resources, Methodology, Conceptualization.

Declaration of competing interest

The authors declare that they have no known competing financial interests or personal relationships that could have appeared to influence the work reported in this paper.

Acknowledgement

The authors gratefully acknowledge the financial support from the China Scholarship Council (No. CSC202006950073).

Appendix

Considering linear elastic material behaviour and a plane stress condition, the SED can be calculated as [62,64]:

$$S = \frac{1}{2}(\sigma_{11}\varepsilon_{11} + \sigma_{22}\varepsilon_{22} + 2\sigma_{12}\varepsilon_{12}) \quad (12)$$

where σ_{ij} and ε_{ij} $(i, j = 1, 2)$ indicate the stress and strain components parallel or transverse to the fibre orientation. For a unidirectional lamina, the stress components can be calculated based on Classical Laminate Theory (CLT) [65]:

$$\sigma_{11} = \frac{E_1}{1 - \upsilon_{12}\upsilon_{21}}(\varepsilon_{11} + \upsilon_{21}\varepsilon_{22}) \quad (13)$$

$$\sigma_{22} = \frac{E_2}{1 - \upsilon_{12}\upsilon_{21}}(\varepsilon_{22} + \upsilon_{12}\varepsilon_{11}) \quad (14)$$

$$\sigma_{12} = 2G_{12}\varepsilon_{12} \quad (15)$$

where E_i and υ_{ij} $(i, j = 1, 2)$ are the elastic modulus and Poisson's ratios along fibre direction and transverse to fibre direction, respectively.

The calculation of SED using Eq. (13)~Eq. (15) is based on a local coordinate system aligning with the fibre direction. For MD laminates, the transformation of the elastic modulus and Poisson's ratio of an angled ply should be calculated as follows:

$$\frac{\upsilon_{xy}}{E_x} = \frac{\upsilon_{yx}}{E_y} = \frac{\cos\theta^2}{E_1}(\cos\theta^2\upsilon_{12} - \sin\theta^2) + \frac{\sin\theta^2}{E_2}(\sin\theta^2\upsilon_{21} - \cos\theta^2) + \frac{\sin\theta^2\cos\theta^2}{G_{12}} \quad (16)$$

$$\frac{1}{E_x} = \frac{\cos\theta^2}{E_1}(\cos\theta^2 - \sin\theta^2\upsilon_{12}) + \frac{\sin\theta^2}{E_2}(\sin\theta^2 - \cos\theta^2\upsilon_{21}) + \frac{\sin\theta^2\cos\theta^2}{G_{12}} \quad (17)$$

$$\frac{1}{E_y} = \frac{\sin\theta^2}{E_1}(\sin\theta^2 - \cos\theta^2\upsilon_{12}) + \frac{\cos\theta^2}{E_2}(\cos\theta^2 - \sin\theta^2\upsilon_{21}) + \frac{\sin\theta^2\cos\theta^2}{G_{12}} \quad (18)$$

$$\frac{1}{G_{xy}} = \frac{4\sin\theta^2\cos\theta^2}{E_1}(1 + \upsilon_{12}) + \frac{4\sin\theta^2\cos\theta^2}{E_2}(1 + \upsilon_{21}) + \frac{(\sin\theta^2 - \cos\theta^2)^2}{G_{12}} \quad (19)$$

where E_i and υ_{ij} $(i, j = x, y)$ are the elastic modulus and Poisson's ratios in a global coordinate system. θ is the angle between the fibre orientation and the longitudinal direction of delamination growth.

The equivalent engineering constants for a specific MD laminates can be calculated based on the rule of mixture, as shown in Fig. A.1 where E_i^{eqv} and $\upsilon_{12/21}^{eqv}$ indicate the equivalent elastic modulus and Poisson's ratios for the laminate. ρ^i is the proportion of kth layer in terms of volume.

By integrating Eq. (16)~Eq. (10) in to Eq. (13)~Eq. (15), the eSED can then be calculated using Eq. (1).

Data availability

The data underlying this paper is available for download from: https://doi.org/10.4121/72b67fbb-dd92-41b0-8d16-bf7679df01b0.v1.

References

[1] de Morais AB, de Moura MF. Evaluation of initiation criteria used in interlaminar fracture tests. Eng Fract Mech 2006;73(16):2264–76. http://dx.doi.org/10.1016/j.engfracmech.2006.05.003.

[2] Wisnom MR. The role of delamination in failure of fibre-reinforced composites. Phil Trans R Soc A 2012;370(1965):1850–70. http://dx.doi.org/10.1098/rsta.2011.0441, arXiv:https://royalsocietypublishing.org/doi/pdf/10.1098/rsta.2011.0441.

[3] ISO-15114. Determination of the mode II fracture resistance for unidirectionally reinforced materials using the calibrated end-loaded split test and an eefective crack length approach. Int Standards 2014.

[4] ASTM D6671M. Standard test method for mixed mode I-Mode II interlaminar fracture toughness of unidirectional fiber reinforced polymer matrix composites. ASTM 2006;15. http://dx.doi.org/10.1520/D6671.

[5] ASTM D7905. Standard test method for determination of the mode II interlaminar fracture toughness of unidirectional fiber-reinforced polymer matrix composites. ASTM 2014;1–18. http://dx.doi.org/10.1520/D7905.

[6] Mognhod Bezzie Y, Paramasivam V, Tilahun S, Selvaraj SK. A review on failure mechanisms and analysis of multidirectional laminates. Mater Today: Proc 2021;46:7380–8. http://dx.doi.org/10.1016/j.matpr.2020.12.1121, 3rd International Conference on Materials, Manufacturing and Modelling.

[7] Bin Mohamed Rehan MS, Rousseau J, Fontaine S, Gong XJ. Experimental study of the influence of ply orientation on DCB mode-I delamination behavior by using multidirectional fully isotropic carbon/epoxy laminates. Compos Struct 2017;161:1–7. http://dx.doi.org/10.1016/j.compstruct.2016.11.036.

[8] Ramji A, Xu Y, Yasaee M, Grasso M, Webb P. Delamination migration in CFRP laminates under mode I loading. Compos Sci Technol 2020;190(June 2019):108067. http://dx.doi.org/10.1016/j.compscitech.2020.108067.

[9] Carraro PA, Maragoni L, Quaresimin M. Stiffness degradation of symmetric laminates with off-axis cracks and delamination: an analytical model. Int J Solids Struct 2021;213:50–62. http://dx.doi.org/10.1016/j.ijsolstr.2020.12.013.

[10] Pourahmadi E, Shadmehri F, Ganesan R. Interlaminar shear strength of carbon/PEEK thermoplastic composite laminate: Effects of in-situ consolidation by automated fiber placement and autoclave re-consolidation. Composites B 2024;269:111104. http://dx.doi.org/10.1016/j.compositesb.2023.111104.
[11] Huang Y, Lv X, Huo H, Zhang B, Peng G, Ge J, et al. Interlaminar reinforced carbon fiber/epoxy composites by electrospun ultrafine hybrid fibers. Composites B 2024;281:111578. http://dx.doi.org/10.1016/j.compositesb.2024.111578.
[12] Hu P, Dias MA, Budzik MK. Geometric tunability of interlaminar resistance. Composites B 2024;287:111839. http://dx.doi.org/10.1016/j.compositesb.2024.111839.
[13] Zhao L, Gong Y, Zhang J, Chen Y, Fei B. Simulation of delamination growth in multidirectional laminates under mode I and mixed mode i/II loadings using cohesive elements. Compos Struct 2014;116(1):509–22. http://dx.doi.org/10.1016/j.compstruct.2014.05.042.
[14] Pichler N, Herr M, Botsis J, Herráez M, Botsis J. Mixed-mode fracture response of anti-symmetric laminates: Experiments and modelling. Composites B 2020;197(May). http://dx.doi.org/10.1016/j.compositesb.2020.108089.
[15] Herráez M, Pichler N, Pappas GA, Blondeau C, Botsis J. Experiments and numerical modelling on angle-ply laminates under remote mode II loading. Composites A 2020;134(March):105886. http://dx.doi.org/10.1016/j.compositesa.2020.105886.
[16] Gong Y, Xia K, Wang Y, Zhao L, Zhang J, Hu N. A semi-analytical model for the mode II fracture toughness of multidirectional composite laminates. Thin-Walled Struct 2023;182(December 2021):110235. http://dx.doi.org/10.1016/j.tws.2022.110235.
[17] Cintra GG, Vieira JD, Cardoso DC, Keller T. Mode I and mode II fracture behavior in pultruded glass fiber-polymer – experimental and numerical investigation. Composites B 2023;266(June):110988. http://dx.doi.org/10.1016/j.compositesb.2023.110988.
[18] Leciñana I, Renart J, Turon A, Zurbitu J, Tijs BH. Characterization and analysis of the mode I interlaminar fatigue behaviour of thermoplastic composites considering R-curve effects. Eng Fract Mech 2023;286(July). http://dx.doi.org/10.1016/j.engfracmech.2023.109273.
[19] Kotrotsos A, Geitona A, Kostopoulos V. On the mode I and mode II fatigue delamination growth of CFRPs modified by electrospun bis-maleimide resin. Compos Sci Technol 2023;237(March):110000. http://dx.doi.org/10.1016/j.compscitech.2023.110000.
[20] Chen Y, Liu K, Xu Z, Liu H, Lißner M, Erice B, Petrinic N. A comprehensive experimental investigation of the rate-dependent interlaminar delamination behaviour of CFRP composites. Composites B 2023;261:110788. http://dx.doi.org/10.1016/j.compositesb.2023.110788.
[21] Hu P, Li X, Lubineau G. Prediction of a complex delamination front using a general cohesive model. Compos Sci Technol 2023;233(November 2022):109911. http://dx.doi.org/10.1016/j.compscitech.2023.109911.
[22] Gong Y, Hou Y, Zhao L, Li W, Zhang J, Hu N. A modified mode I cohesive zone model for the delamination growth in DCB laminates with the effect of fiber bridging. Int J Mech Sci 2020;176(August 2019):105514. http://dx.doi.org/10.1016/j.ijmecsci.2020.105514.
[23] Chatziathanasiou T, Soete J, Vanhulst J, Carrella-Payan D, Gorbatikh L, Mehdikhani M. In-situ X-ray computed tomography of mode I delamination in carbon-epoxy composites: The effect of the interface ply orientation. Composites B 2023;260(April):110761. http://dx.doi.org/10.1016/j.compositesb.2023.110761.
[24] Daneshjoo Z, Shokrieh MM, Fakoor M, Alderliesten RC. A new mixed mode i/II failure criterion for laminated composites considering fracture process zone. Theor Appl Fract Mech 2018;98(May):48–58. http://dx.doi.org/10.1016/j.tafmec.2018.09.004.
[25] Sommer J, Hajikazemi M, De Baere I, Van Paepegem W. Experimental and numerical fatigue damage characterization in multidirectional thermoplastic glass/polypropylene laminates based on in-situ damage observations. Composites B 2023;267:111028. http://dx.doi.org/10.1016/j.compositesb.2023.111028.
[26] Greenhalgh ES, Rogers C, Robinson P. Fractographic observations on delamination growth and the subsequent migration through the laminate. Compos Sci Technol 2009;69(14):2345–51. http://dx.doi.org/10.1016/j.compscitech.2009.01.034.
[27] McQuien JS, Hoos KH, Ferguson LA, Iarve EV, Mollenhauer DH. Geometrically nonlinear regularized extended finite element analysis of compression after impact in composite laminates. Composites A 2020;134(December 2019):105907. http://dx.doi.org/10.1016/j.compositesa.2020.105907.
[28] Selvaraj J, Kawashita LF, Melro AR, Hallett SR. Efficient sublaminate-scale impact damage modelling with higher-order elements in explicit integration. Composites A 2023;172(December 2022):107560. http://dx.doi.org/10.1016/j.compositesa.2023.107560.
[29] Canal LP, Alfano M, Botsis J. A multi-scale based cohesive zone model for the analysis of thickness scaling effect in fiber bridging. Compos Sci Technol 2017;139:90–8. http://dx.doi.org/10.1016/j.compscitech.2016.11.027.
[30] Hashemi S, Kinloch A, Williams J. The effects of geometry, rate and temperature on the mode I, mode II and mixed-mode I/II interlaminar fracture of carbon-fibre/poly(ether-ether ketone) composites. J Compos Mater 1990;24(9):918–56. http://dx.doi.org/10.1177/002199839002400902.
[31] Garulli T, Catapano A, Fanteria D, Huang W, Jumel J, Martin E. Experimental assessment of fully-uncoupled multi-directional specimens for mode I delamination tests. Compos Sci Technol 2020;200(August):108421. http://dx.doi.org/10.1016/j.compscitech.2020.108421.
[32] Völkerink O, Koord J, Petersen E, Hühne C. Holistic determination of physical fracture toughness values and numerical parameters for delamination analysis considering multidirectional-interfaces. Composit C: Open Access 2022;8(March). http://dx.doi.org/10.1016/j.jcomc.2022.100277.
[33] Jadhav P, Yella G, Azmeera A, Lande C. Mode II- delamination modeling in multi-directional laminates using cohesive zone methodology under static and dynamic loading. Mater Today: Proc 2023;1–8. http://dx.doi.org/10.1016/j.matpr.2023.01.227.
[34] Delta-tech. Matrix technical data sheet - DT120 versatile high toughness epoxy matrix. Tech. rep, Delta-tech; 2015.
[35] Hahn P, Channammagari H, Imbert M, May M. High-rate mode II fracture toughness testing of polymer matrix composites using the transverse crack tension (TCT) test. Composites B 2022;233:109636. http://dx.doi.org/10.1016/j.compositesb.2022.109636.
[36] Wang C, Vassilopoulos AP, Keller T. Numerical investigation of two-dimensional mode-II delamination in composite laminates. Composites A 2024;179(January):108012. http://dx.doi.org/10.1016/j.compositesa.2024.108012.
[37] Vinciquerra AJ, Davidson BD, Schaff JR, Smith SL. Determination of the mode II fatigue delamination toughness of laminated composites. J Reinf Plast Compos 2002;21(7):663–77. http://dx.doi.org/10.1177/0731684402021007473.
[38] Perez CL, Davidson BD. Evaluation of precracking methods for the end-notched flexure test. AIAA J 2007;45(11):2603–11. http://dx.doi.org/10.2514/1.24188.
[39] Blackman BR, Brunner AJ, Williams JG. Mode II fracture testing of composites: a new look at an old problem. Eng Fract Mech 2006;73(16):2443–55. http://dx.doi.org/10.1016/j.engfracmech.2006.05.022.
[40] Pérez-Galmés M, Renart J, Sarrado C, Rodríguez-Bellido A, Costa J. A data reduction method based on the J-integral to obtain the interlaminar fracture toughness in a mode II end-loaded split (ELS) test. Composites A 2016;90:670–7. http://dx.doi.org/10.1016/j.compositesa.2016.08.020.
[41] Amaral L. Towards fundamental understanding of interlaminar ply delamination growth under mode II and mixed-mode loading [Ph.D. thesis], Delft University of Technology; 2018, p. 289. http://dx.doi.org/10.4233/uuid.
[42] Gong Y, Zhao L, Zhang J, Hu N, Zhang C. Development of a standardized test procedure and an improved data reduction method for the mixed-mode i/II delamination in composite laminates. Compos Sci Technol 2021;201(October 2020):108488. http://dx.doi.org/10.1016/j.compscitech.2020.108488.
[43] Li X, Monticeli F, Pascoe J-A, Mosleh Y. Interlaminar fracture behaviour of emerging laminated-pultruded CFRP plates for wind turbine blades. Eng Fract Mech 2024;308:110353. http://dx.doi.org/10.1016/j.engfracmech.2024.110353.
[44] Hashemi S, Kinloch A, Williams JG. The analysis of interlaminar fracture in uniaxial fibre-polymer composites. Proc R Soc A 1990;427(1872):173–99. http://dx.doi.org/10.1098/rspa.1990.0007.
[45] Smiley A, Pipes R. Rate effects on mode I interlaminar fracture toughness in composite materials. J Compos Mater 1987;21(7):670–87. http://dx.doi.org/10.1177/002199838702100706.
[46] Saeedifar M, Fotouhi M, Ahmadi Najafabadi M, Hosseini Toudeshky H, Minak G. Prediction of quasi-static delamination onset and growth in laminated composites by acoustic emission. Composites B 2016;85:113–22. http://dx.doi.org/10.1016/j.compositesb.2015.09.037.
[47] Saeedifar M, Zarouchas D. Damage characterization of laminated composites using acoustic emission: A review. Composites B 2020;195(January):108039. http://dx.doi.org/10.1016/j.compositesb.2020.108039.
[48] Biagini D, Pascoe J-A, Alderliesten R. Investigation of compression after impact failure in carbon fiber reinforced polymers using acoustic emission. J Compos Mater 2023;57(10):002199832311638. http://dx.doi.org/10.1177/00219983231163853.
[49] Cesari F, Dal Re V, Minak G, Zucchelli A. Damage and residual strength of laminated carbon-epoxy composite circular plates loaded at the centre. Composites A 2007;38(4):1163–73. http://dx.doi.org/10.1016/j.compositesa.2006.04.013.
[50] Bakhtiary Davijani AA, Hajikhani M, Ahmadi M. Acoustic emission based on sentry function to monitor the initiation of delamination in composite materials. Mater Des 2011;32(5):3059–65. http://dx.doi.org/10.1016/j.matdes.2011.01.010.
[51] Wang C, Vassilopoulos AP, Keller T. Experimental investigation of two-dimensional mode-II delamination in composite laminates. Composites A 2023;173(March):107666. http://dx.doi.org/10.1016/j.compositesa.2023.107666.
[52] Krishnappa S, Gururaja S. Compressive failure mechanisms in unidirectional fiber reinforced polymer composites with embedded wrinkles. Composites B 2024;284:111688. http://dx.doi.org/10.1016/j.compositesb.2024.111688.
[53] Akbolat MÇ, Katnam KB, Soutis C, Potluri P, Sprenger S, Taylor J. On mode-I and mode-II interlaminar crack migration and R-curves in carbon/epoxy laminates with hybrid toughening via core-shell rubber particles and thermoplastic micro-fibre veils. Composites B 2022;238:109900. http://dx.doi.org/10.1016/j.compositesb.2022.109900.

[54] Carpinteri A, Cornetti P, Barpi F, Valente S. Cohesive crack model description of ductile to brittle size-scale transition: dimensional analysis vs. renormalization group theory. Eng Fract Mech 2003;70(14):1809–39. http://dx.doi.org/10.1016/S0013-7944(03)00126-7, Cohesive Models.

[55] Ding J, Xu W. Determination of mode I interlaminar fracture toughness of composite by a wedge-insert double cantilever beam and the nonlinear J integral. Compos Sci Technol 2021;206:108674. http://dx.doi.org/10.1016/j.compscitech.2021.108674.

[56] Erives R, Sørensen BF, Goutianos S. Extraction of mix-mode cohesive laws of a unidirectional composite undergoing delamination with large-scale fibre bridging. Composites A 2023;165(November 2022):107346. http://dx.doi.org/10.1016/j.compositesa.2022.107346.

[57] Chen Q, Wu F, Jiang Z, Zhang H, Yuan J, Xiang Y, et al. Improved interlaminar fracture toughness of carbon fiber/epoxy composites by a combination of extrinsic and intrinsic multiscale toughening mechanisms. Composites B 2023;252:110503. http://dx.doi.org/10.1016/j.compositesb.2023.110503.

[58] Hu P, Tao R, Li X, Lubineau G. Decomposing the coupling damage in mode I multidirectional delamination. Compos Sci Technol 2022;229(April):109684. http://dx.doi.org/10.1016/j.compscitech.2022.109684.

[59] Koord J, Hühne C. Effect of low temperature on interlaminar fracture toughness of multi-directional CFRP and CFRP-steel interfaces. Composites B 2024;111540. http://dx.doi.org/10.1016/j.compositesb.2024.111540.

[60] Sacchetti F, Grouve WJ, Warnet LL, Fernandez Villegas I. Interlaminar fracture toughness of 5HS carbon/PEEK laminates. a comparison between DCB, ELS and mandrel peel tests. Polym Test 2018;66(October 2017):13–23. http://dx.doi.org/10.1016/j.polymertesting.2017.12.005.

[61] Ding Z, Gong Y, Wang Z, Zhang Y, Hu N. A semi-analytical method for the determination of fracture toughness and bridging law in ELS test. Theor Appl Fract Mech 2023;123(November 2022):103712. http://dx.doi.org/10.1016/j.tafmec.2022.103712.

[62] Amaral L, Alderliesten R, Benedictus R. Towards a physics-based relationship for crack growth under different loading modes. Eng Fract Mech 2018;195:222–41. http://dx.doi.org/10.1016/j.engfracmech.2018.04.017.

[63] Sih GC, Macdonald B. Fracture mechanics applied to engineering problems-strain energy density fracture criterion. Eng Fract Mech 1974;6(2):361–86. http://dx.doi.org/10.1016/0013-7944(74)90033-2.

[64] Boresi AP, Schmidt RJ, Sidebottom OM. Advanced mechanics of fluids, vol. 12, Oxford Univerisity Press; 1959, p. 54–5. http://dx.doi.org/10.1063/1.3060940.

[65] Hancox N. Engineering mechanics of composite materials. Wiley New York; 1996, p. 114. http://dx.doi.org/10.1016/s0261-3069(97)87195-6.